

# Effect of Turbulence and Diffusional–Thermal Instability on Hydrogen-Rich Syngas Turbulent Premixed Flame

Guo-Peng Zhang, Guo-Xiu Li,\* Hong-Meng Li,\* and Jian-Bin Cao

As a kind of fuel with low-carbon emissions, hydrogen-rich syngas has a large resource potential and is a promising alternative energy resource. A series of experiments in a constant volume combustion bomb are carried out to investigate the effects of turbulence and diffusional–thermal (DT) instability on a hydrogen-rich syngas turbulent premixed flame. The flow field in the constant volume combustion bomb is calibrated, and the turbulent flow field's homogeneity and isotropy were investigated. The effects of different speeds of fan (1366–4273 rpm), hydrogen fractions (55%–95%), pressures (1.0–3.0 bar), and equivalence ratios (0.6–1.0) on the hydrogen-rich syngas turbulent premixed flame are studied. According to the analyses, the flow field in the experimental device exhibits good homogeneous and isotropic characteristics. With the increase of turbulence intensity, equivalence ratio, hydrogen fraction, or pressure, the turbulent flame propagation speed increases gradually. As the hydrogen fraction increases or the equivalence ratio decreases, the effective Lewis number decreases, and the effect of DT instability on the flame increases. The research in this article is crucial for the clean and efficient utilization of hydrogen-rich syngas and the design of related burners.

emissions from hydrogen-rich mixed fuels.<sup>[6]</sup> As a kind of fuel with low carbon emissions, hydrogen-rich syngas has extensive resource availability and is also a promising alternative energy resource.<sup>[7–9]</sup> In addition, most of the combustion phenomenon in actual power plants constitutes turbulent premixed combustion. Therefore, the research of turbulent premixed combustion is very important for the clean and efficient utilization of fossil fuels and for the design and development of industrial burners.<sup>[10–14]</sup>

The research on the propagation properties of turbulent premixed flame is also the focus many scholars' works.<sup>[15,16]</sup> The common experimental devices of turbulent premixed flame are jet burners,<sup>[17–19]</sup> constant volume burners,<sup>[20–22]</sup> swirl burners,<sup>[23,24]</sup> and hedge flame burners.<sup>[25]</sup> Among them, the constant volume bomb can create a homogeneous isotropic turbulent flow field in the bomb, which is very important for analyzing the various characteristics of tur-

bulent premixed flame. However, the shape of constant volume bomb and the size and number of fans used in various works are different. Due to this reason, the turbulence intensity and the length scale created in a constant volume bomb are not the same in these works. **Table 1** lists the constant volume combustion devices used by different scholars while studying the turbulent premixed flames.

Compared with the constant volume bomb in Table 1, the spherical constant volume bomb used in this article can greatly reduce the influence of pressure waves on combustion. In addition, the pyramid shaped fan inside the constant volume combustion bomb in this article can better construct a homogeneity and isotropy flow field, which will be discussed in the second and third section.

The inherent instabilities are the internal factor affecting the turbulent premixed flame, and mainly includes Darrieus–Landau (DL) instability<sup>[26,27]</sup> and diffusional–thermal (DT) instability.<sup>[28,29]</sup> The turbulent premixed flame front evolves as a direct result of the effect of turbulence and the inherent instabilities on the turbulent premixed flame.<sup>[30–33]</sup> In a spherical premixed flame, the flame front usually maintains a high degree of flatness and smoothness for a small radius. The stretch rate of a flame gradually decreases as it propagates in a turbulent environment, and the disturbance of the flame front develops to varying degrees, resulting in the formation of folds and cellular structures in the flame front.


## 1. Introduction

Chinese government has proposed to reach the peak of CO<sub>2</sub> emissions by 2030 and to achieve the goal of carbon neutralization by 2060.<sup>[1]</sup> With the goal of “double carbon” in China, the exploration of alternative energy resources has sped up in the country.<sup>[2–4]</sup> For hydrogen-rich fuels, an increase in hydrogen content will significantly reduce CO<sub>2</sub> emissions.<sup>[5]</sup> In addition, there will be a significant improvement in nitrogen oxide

G.-P. Zhang, G.-X. Li, H.-M. Li, J.-B. Cao  
School of Mechanical, Electronic and Control Engineering  
Beijing Jiaotong University  
Beijing 100044, China  
E-mail: gxli@bjtu.edu.cn; hongmengli@bjtu.edu.cn

G.-P. Zhang, G.-X. Li, H.-M. Li, J.-B. Cao  
Beijing Key Laboratory of New Energy Vehicle Powertrain Technology  
Beijing Jiaotong University  
Beijing 100044, China

G.-P. Zhang  
State Key Laboratory of High Temperature Gas Dynamics  
Institute of Mechanics  
Chinese Academy of Sciences  
Beijing 100190, China

 The ORCID identification number(s) for the author(s) of this article can be found under <https://doi.org/10.1002/ente.202300895>.

DOI: 10.1002/ente.202300895

**Table 1.** Constant volume combustion devices for studying the turbulent premixed flames.

References	Vessel shape	Vessel size [mm]	Fan diameter [mm]	Number of fans	Maximum fan speed [rpm]	Maximum turbulence intensity [ $\text{m s}^{-1}$ ]	Turbulence integral length scale [mm]
Semenov, (1965) <sup>[53]</sup>	Spherical	$D = 97$	–	4	7000	10	–
Fansler et al., (1990) <sup>[54]</sup>	Cylindrical	$D = 260, l = 260$	135	4	2500	2.2	25–40
Sick et al., (2001) <sup>[55]</sup>	Spherical	$D = 58$	48	4	7000	1.8	6.9
Smallbone et al., (2006) <sup>[56]</sup>	Intersection of three cylinders	$D = 265$	–	2	–	3.5	1.2
Kitagawa et al., (2008) <sup>[48]</sup>	Spherical	$D = 406$	–	2	–	1.59	10.3
Weiβ et al., (2008) <sup>[45]</sup>	Spherical	$D = 118$	45	8	10 000	3.5	3.9
Liu et al., (2011) <sup>[57]</sup>	Cuboidal	$l = 150$	116	2	7620	4.5	15–48
Ravi et al., (2013) <sup>[46]</sup>	Cylindrical	$D = 305, l = 356$	76.2	4	8300	3.5	20–27
Galmiche et al., (2014) <sup>[49]</sup>	Spherical	$D = 200$	40	6	15 000	2.8	3.4
Chaudhuri et al., (2015) <sup>[51]</sup>	Cylindrical	$D = 114, l = 127$	69	4	4000	2.3	–
Goulier et al., (2017) <sup>[58]</sup>	Spherical	$D = 563$	–	8	5000	4	45–52
Bradley et al., (2019) <sup>[59]</sup>	Spherical	$D = 380$	–	4	10 000	12	20
Jiang et al., (2019) <sup>[60]</sup>	Spherical	$D = 380$	90	4	3408	1.31	–
Zhao et al., (2020) <sup>[47]</sup>	Cylindrical	$D = 345, l = 307$	114	4	10 000	3.62	10.6–16.1
Mannaa et al., (2021) <sup>[61]</sup>	Spherical	$D = 440$	70	4	6000	4.7	23.5

Jin et al.<sup>[34]</sup> found that the propagation speed of turbulent flame in medium- and low-intensity turbulence is closely related to DT instability of the  $\text{CH}_4/\text{H}_2$  mixture. Creta et al.<sup>[35]</sup> found that the flame's propagation speed that was affected by additional DT instability was much higher than that affected by DL instability alone. Li et al.<sup>[36]</sup> found that DT instability first decreased, and then remained stable as propane concentration was increased in the investigation of hydrogen/propane premixed flame instability. Dinesh et al.<sup>[37,38]</sup> discovered that the development of the cellular structure was mainly controlled by turbulence; however, the acceleration of flame was still affected by preferential diffusion in the lean premixed flame under strong turbulence and high pressure. Vu et al.<sup>[39]</sup> found that Lewis number was not sensitive to changes in initial pressure. In addition, they also found that both DL instability and DT instability increased with the increase of hydrogen content in the reactant mixture. Berger et al.<sup>[40,41]</sup> found that the DT instability resulted from the strong differential diffusion caused by low Lewis number of hydrogen, which resulted in a change in local equivalence ratio and thus a change in reaction rate along the flame front. Kadowaki et al.<sup>[42]</sup> found that, when the Lewis number was less than unity, the cellular flame front became more unstable, while the diffusional–thermal effect had a great impact on the instability of flame. Liu et al.<sup>[43]</sup> investigated that DT instability played a strong role in the wrinkled flamelet and corrugated flamelet regimes, while the effect was weak in the thin reaction zone. Pashchenko<sup>[44]</sup> found through comparative analysis of 2D and 3D hydrogen premixed flames that solving combustion problems using 2D methods can lead to significant deviations from actual results, while the 3D method can be in good agreement with the experimental results and can accurately judge the propagation characteristics and stability of the premixed flame.

Through the research of the aforementioned scholars, it can be found that the influence of DL instability on flame is small under low pressure, so this paper mainly analyzes the influence

of DT instability. In addition, due to the inherent instability of hydrogen-rich syngas turbulent premixed flame, the kinetic mechanism of the flame propagation under turbulent flow is very complex. The relative effects of turbulence and inherent instabilities of flames vary under different turbulence intensities, and scholars have not conducted in-depth research on this topic. Exploring the coupling effect of turbulence and DT instability of flame on the propagation of hydrogen-rich syngas turbulent premixed flame has important guiding significance for revealing the essence of turbulent combustion of syngas and its efficient and clean utilization. In this article, the turbulent premixed flame of hydrogen-rich syngas was studied at temperature of 298 K under different fan speeds (1366–4273 rpm), different hydrogen fractions (55–95%), different pressures (1.0–3.0 bar), and different equivalence ratios (0.6–1.0).

## 2. Experimental Section

The experimental apparatus used to study the hydrogen-rich syngas turbulent premixed combustion mainly consisted of five parts: constant volume bomb, turbulence building unit, intake and exhaust unit, synchronous trigger and ignition unit, and image acquisition unit. The working principle of the experimental setup can be found in one of our previous works.<sup>[22]</sup>

The turbulence building unit is the key of the experimental setup, and can create a stable and homogeneous isotropic turbulent flow field in the constant volume bomb. The four motors were DC brushed motors with the each having a rated power and a maximum speed of 2 kW and 10 000 rpm, respectively. Compared with the three-phase AC motor, the speed of the DC motor was more stable and could also be controlled more easily. To ensure the airtightness of the constant volume bomb, the DC motor was not directly connected with the fan shaft. Instead, the motor drove the fan in the combustion bomb through a magnetic coupling. The four fans in the experimental

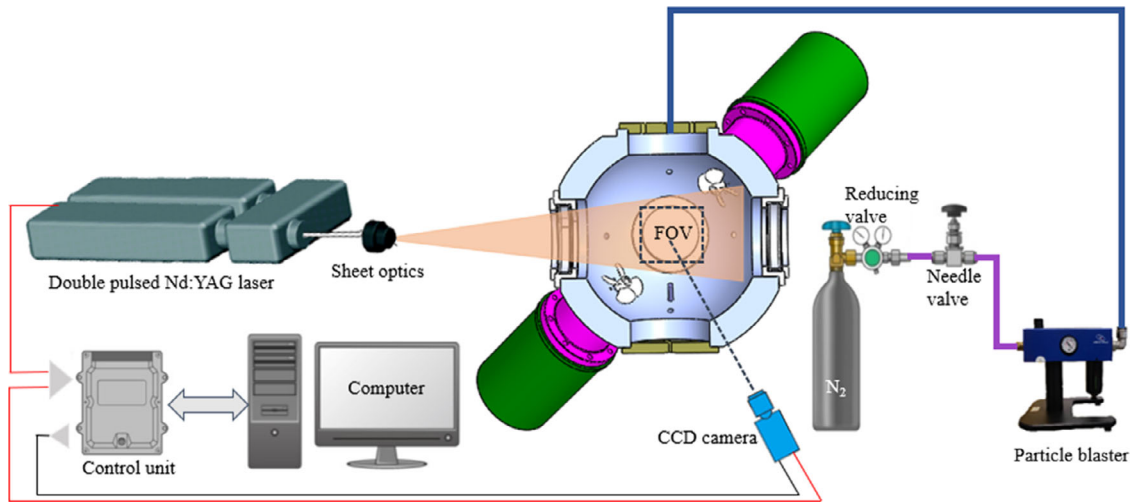


**Figure 1.** Schematic of the particle image velocimetry (PIV) measurement system.

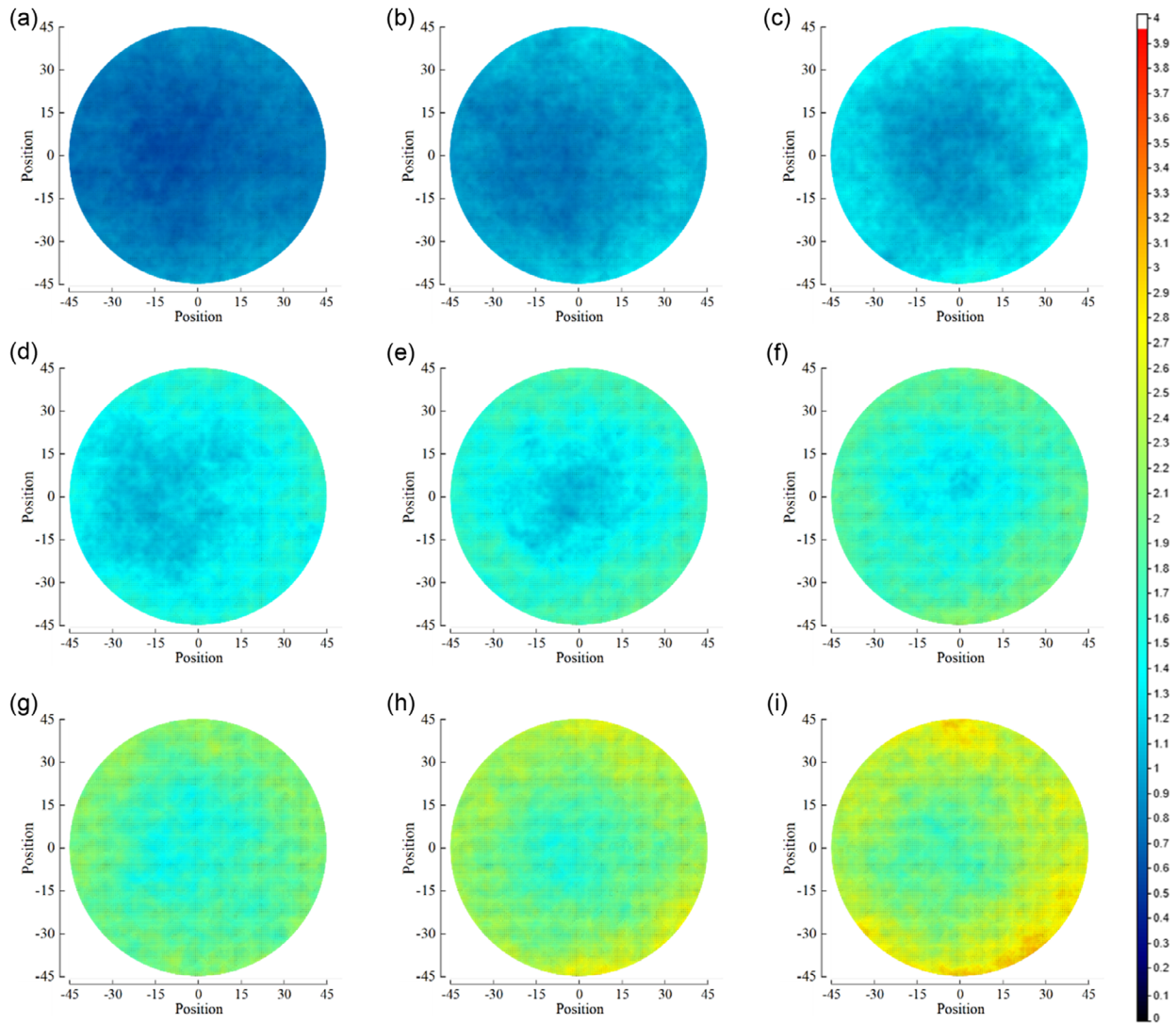


**Figure 2.** Mean field of turbulent fluctuating velocity under the pressure of 1.0 bar. a) 1366 rpm; b) 1740 rpm; c) 2103 rpm; d) 2427 rpm; e) 2832 rpm; f) 3212 rpm; g) 3559 rpm; h) 3907 rpm; and i) 4273 rpm.

setup were all manufactured using 3D printing, which ensured not only the strength of the fan, but also resulted in a consistent size and shape of the fans. The diameter of each fan was 100 mm.

In this article, the turbulence in the constant volume bomb was generated due to the rotation of the fan, which was driven by the motor. Therefore, it was necessary to measure the turbulence field in the constant volume bomb. A number of turbulent flow field calibration experimental setups were built (see Figure 1). The particle image velocimetry (PIV) setups mainly consisted of four parts: high-energy dual-cavity Nd:YAG laser, charge coupled device camera, tracer particle generator, and image acquisition and data processing unit. The duration of the application of laser was less than 10 ns. After the laser was passed through the optical

guide arm, the cylindrical concave lens was used to convert it from a point light source to a 1.0 mm thin sector light source. During the measurement of turbulent flow field, the field of view was round with a radius of 45 mm, and the area of the field of view was enough to measure and evaluate the initial flow field of hydrogen-rich syngas turbulent premixed flame.

In this study, di-ethyl-hexyl-sebacat was used as a tracer. A particle generator was used to create the tracer particles, which had a diameter of about 1.0  $\mu\text{m}$  and were transported to the bomb using nitrogen. The fan was turned on once the particles were in a quasi-steady state, and then the 15 Hz data gathering procedure was started. Three groups of 300 image pairs were acquired for each working condition, totaling 900 image pairs, which was thought to

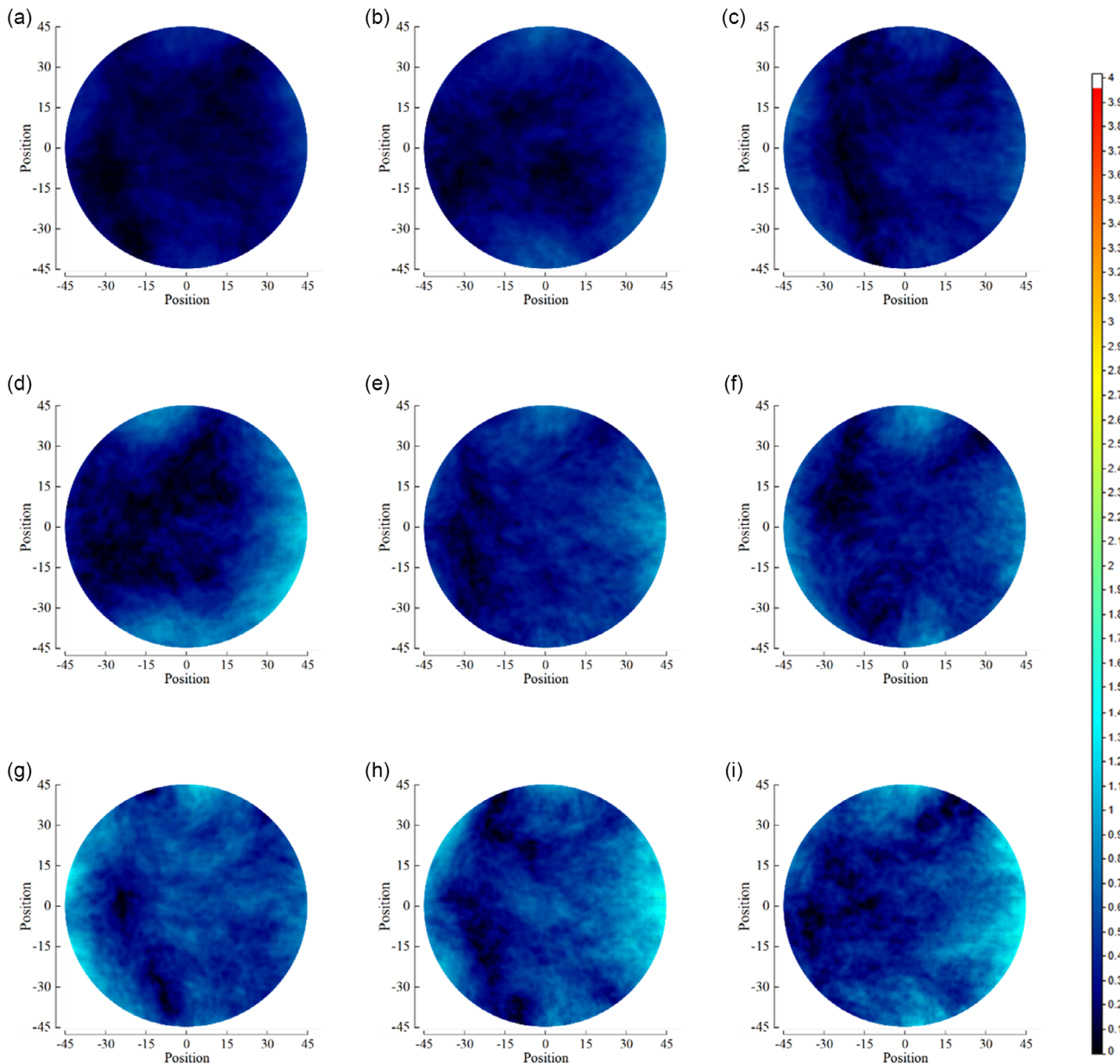


**Figure 3.** Turbulent mean velocity field under the pressure of 1.0 bar. a) 1366 rpm; b) 1740 rpm; c) 2103 rpm; d) 2427 rpm; e) 2832 rpm; f) 3212 rpm; g) 3559 rpm; h) 3907 rpm; i) 4273 rpm.

be sufficient to accurately estimate the turbulent flow field. Davis 10.0 software was used to process the cross correlation of particle images. Vector computing used adaptive multichannel vector evaluation technology, while the size of the query window was reduced from  $64 \times 64$  to  $16 \times 16$  pixels, with the overlapping of 75–50%.

### 3. Results and Discussion

#### 3.1. Calibration of the Flow Field

**Figure 2** shows the turbulent fluctuation velocity field at different fan speeds under the pressure of 1 bar to visually evaluate the distribution of turbulent fluctuation velocity. The distribution of the turbulent fluctuation velocity field was roughly circular and stratified. From the center to the edge, the turbulent fluctuation velocity gradually increased. This is mainly because the outside position was closer to the fan and, therefore, had a stronger turbulent fluctuation velocity. In addition, the spatial and operational arrangement of the four fans was reasonable, as evidenced by the turbulent flow field's roughly circular distribution. With the increase of fan speed, the turbulent fluctuation velocity obviously increased.

**Figure 3** shows the mean velocity field at different fan speeds under the pressure of 1 bar to visually evaluate the distribution of turbulent mean velocity. For the turbulent mean velocity field, it is found that the mean velocity at the center of the field of view was very small. The mean velocity expanded to the wall, and increased slightly. However, the overall mean velocity field was much smaller than the fluctuation flow field. With the increase of fan speed, the mean velocity increased slightly.

The velocity vector fields in various image pairs were the initial data collected by PIV. Equation (1) and (2) provide the average velocity components in the two orthogonal directions ( $x, y$ ).

$$\bar{u}(x, y) = \frac{1}{n} \sum_{j=1}^n u_j(x, y) \quad (1)$$

$$\bar{v}(x, y) = \frac{1}{n} \sum_{j=1}^n v_j(x, y) \quad (2)$$

where  $n$  is the total number of image pairs, with a value of 900 in the current work.

The total speed is calculated using Equation (3).

$$\bar{U}(x, y) = \sqrt{\bar{u}(x, y)^2 + \bar{v}(x, y)^2} \quad (3)$$

Equation (4) and (5) determine the root mean square of velocity fluctuation in the two orthogonal directions.

$$u_{\text{RMS}}(x, y) = \sqrt{\frac{1}{n} \sum_{j=1}^n [u_j(x, y) - \bar{u}(x, y)]^2} \quad (4)$$

$$v_{\text{RMS}}(x, y) = \sqrt{\frac{1}{n} \sum_{j=1}^n [v_j(x, y) - \bar{v}(x, y)]^2} \quad (5)$$

**Table 2.** Turbulence intensity at different fan speeds.

$\omega$ [rpm]	$u'$ [ $\text{m s}^{-1}$ ]		
	$P = 1.0$ [bar]	$P = 2.0$ [bar]	$P = 3.0$ [bar]
1366	0.847	0.809	0.814
1740	1.053	1.030	1.033
2103	1.289	1.283	1.252
2427	1.478	1.498	1.485
2832	1.671	1.649	1.658
3212	1.851	1.860	1.860
3559	2.034	2.109	2.079
3907	2.327	2.278	2.305
4273	2.533	2.527	2.532

Equation (6) describes the turbulence intensity.

$$u'(x, y) = \sqrt{\frac{u_{\text{RMS}}(x, y)^2 + v_{\text{RMS}}(x, y)^2}{2}} \quad (6)$$

The turbulent pulsation field was averaged spatially, and the turbulence intensity under different conditions was obtained, as shown in **Table 2**. The fan speed had a direct relationship with the turbulence intensity, which is compatible with the description given in refs. [45–47]. The maximum turbulence intensity in this article could reach  $2.533 \text{ m s}^{-1}$ . Compared with the fan speed, the ambient pressure had no discernible impact on the turbulence intensity.

The integral length scale, which physically depicts the typical size of large-scale eddies in turbulence, is another crucial measure for describing turbulence. Several approaches have been put out in earlier publications<sup>[48,49]</sup> for calculating the integral length scale. Integrating the correlation coefficient of turbulent fluctuation velocity, which is a function of distance between two points, yielded the integral length scale (see Equation (7)–(10)).

$$R_{ux}(\Delta x) = \frac{\langle u_f(x, y, t) u_f(x + \Delta x, y, t) \rangle}{u'_f(t)^2} \quad (7)$$

$$L_{ux} = \int_0^\infty R_{ux}(\Delta x, 0) d(\Delta x) \quad (8)$$

$$R_{vy}(\Delta x) = \frac{\langle v_f(x, y, t) v_f(x + \Delta x, y, t) \rangle}{v'_f(t)^2} \quad (9)$$

$$L_{vy} = \int_0^\infty R_{vy}(\Delta x, 0) d(\Delta x) \quad (10)$$

where  $L_{ux}$  is the longitudinal integral length scale in the  $x$  direction;  $L_{vy}$  is the longitudinal integral length scale in the  $y$  direction;  $R_{ux}(\Delta x)$  and  $R_{vy}(\Delta x)$  are the longitudinal fluctuating velocity correlation coefficients in the  $x$  and  $y$  directions, respectively; and  $u'_f(t)$  is the root mean square of the fluctuation velocity in the entire spatial field. Similarly, the lateral integral length scale can be estimated using a similar method.

**Table 3** depicts the results of the integral length scale under various conditions. Pressure had no effect on the integral length scale, as can be seen. However,  $L_T$  increased with the increase of

**Table 3.** Turbulence integral length scale at different fan speeds.

$\omega$ [rpm]	$L_T$ [mm]		
	$P = 1.0$ [bar]	$P = 2.0$ [bar]	$P = 3.0$ [bar]
1366	9.221	8.674	8.748
1740	11.636	11.407	11.438
2103	13.530	13.490	13.281
2427	14.578	14.670	14.611
2832	15.349	15.273	15.304
3212	15.869	15.891	15.891
3559	16.256	16.383	16.334
3907	16.670	16.615	16.646
4273	16.859	16.854	16.858

fan speed, which is consistent with the results reported in a previous study.<sup>[47]</sup> In addition, the results of Xu et al.<sup>[50]</sup> also showed that the  $L_T$  increased with the increase in fan speed. In actuality,  $L_T$  was likewise zero when the fan speed was zero. As a result,  $L_T$  was found to vary with fan speed.

Considered to be the most basic type of turbulence, homogeneous isotropic turbulence is frequently used as a benchmark for research on the physical characteristics of turbulence.<sup>[49]</sup> Under the conditions of homogeneity and isotropy, the inherent randomness of the actual turbulent flow field can be reduced, so that it is easier to understand the hydrodynamics of turbulent combustion. In this article, to estimate the homogeneity of the turbulent flow field, the homogeneity ratio  $H$  is introduced.  $H$  is defined as the ratio of the local root-mean-square velocity to the spatial root-mean-square velocity in the same direction (see Equation (11) and (12)).

$$H_x = \frac{u_{RMS}(x, y)}{\bar{u}_{RMS}} \quad (11)$$

$$H_y = \frac{v_{RMS}(x, y)}{\bar{v}_{RMS}} \quad (12)$$

where  $H_x$  and  $H_y$  are the homogeneity ratios in the  $x$  and  $y$  directions, respectively.

In general, the turbulence field can be considered to be homogeneous when the homogeneity ratio is within the range of 0.8–1.2.<sup>[47,51]</sup> Figure 4 shows  $H_x$  in the direction of  $y = 0$  under different pressures and fan speeds. The distribution of homogeneity is comparable to how the turbulence intensity gradually grew from the center to the periphery. Under different pressures and fan speeds, the homogeneity ratio of the turbulent field in the  $y = 0$  direction lied within the range of 0.8–1.2, indicating that this region had a good homogeneity. Although there were a few points near the fan that did not lie within the range of 0.8–1.2, the spatial homogeneity of the whole field of view was reasonable. Similarly, Figure 5 shows  $H_y$  in the direction of  $x = 0$  under different pressures and fan speeds. The distribution of  $H_y$  is comparable to how  $H_x$  gradually grew from the center to the periphery. Similarly, under different pressures and fan speeds, the homogeneity ratio of the turbulent field in the direction of  $x = 0$  lied within the range of 0.8–1.2, indicating that the region had a good homogeneity. Combining the results

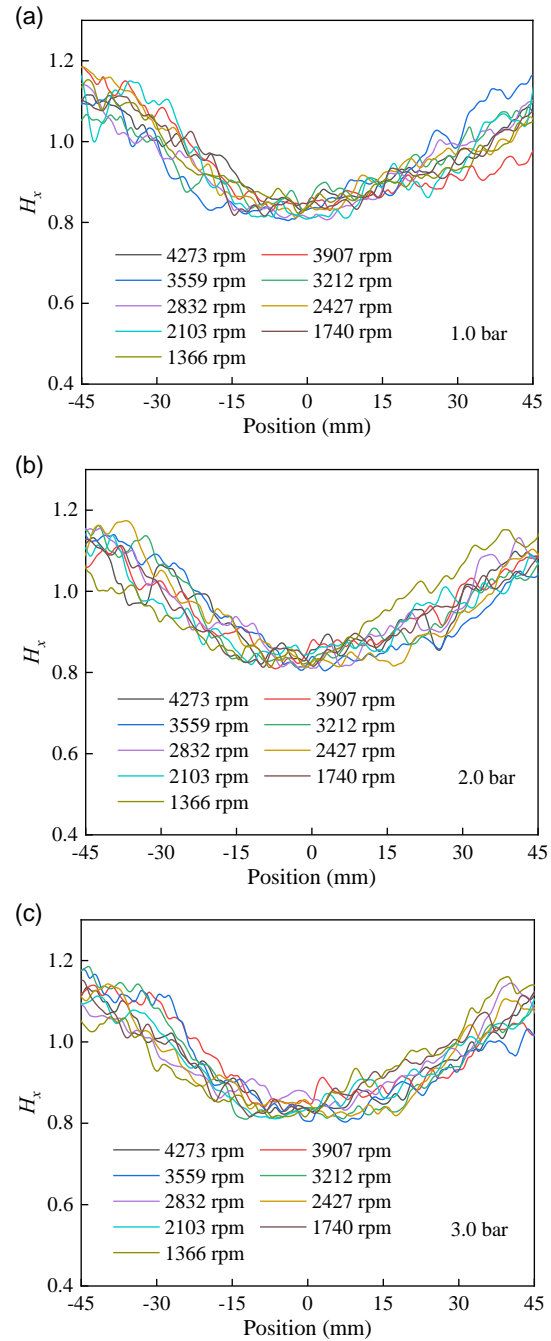


**Figure 4.** Homogeneity ratio in  $y = 0$  direction. a)  $P = 1.0$  bar; b)  $P = 2.0$  bar; and c)  $P = 3.0$  bar.

presented in Figure 4 and 5, it can be seen that the turbulent flow field in the visible range was homogenous.

The isotropic ratio, which is determined by Equation (15), as the ratio of the local-root-mean-square velocity in two vertical directions, is used to measure the isotropy of the turbulent field.

$$I = \frac{u_{RMS}(x, y)}{v_{RMS}(x, y)} \quad (15)$$

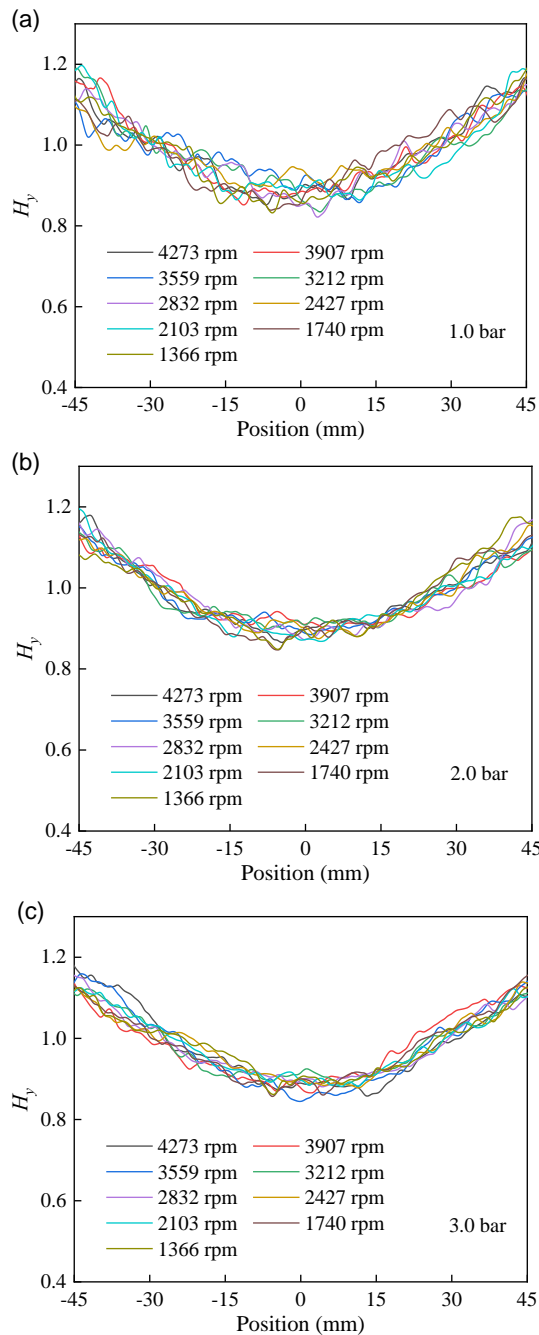


**Figure 5.** Homogeneity ratio in  $x=0$  direction. a)  $P=1.0$  bar; b)  $P=2.0$  bar; and c)  $P=3.0$  bar.

In general, the turbulence field can be considered isotropic when the isotropic ratio lies within the range of 0.9–1.1.<sup>[47,51]</sup>

**Figure 6** shows the isotropic ratio in the whole field of view under different pressures and fan speeds. The majority of the isotropic ratios were focused in the 0.9–1.1 range, demonstrating the isotropy of the turbulence field at various pressures and fan speeds. Although there were a few points that did not lie within the range of 0.9–1.1, the isotropy of the whole field of vision can be considered reasonable.

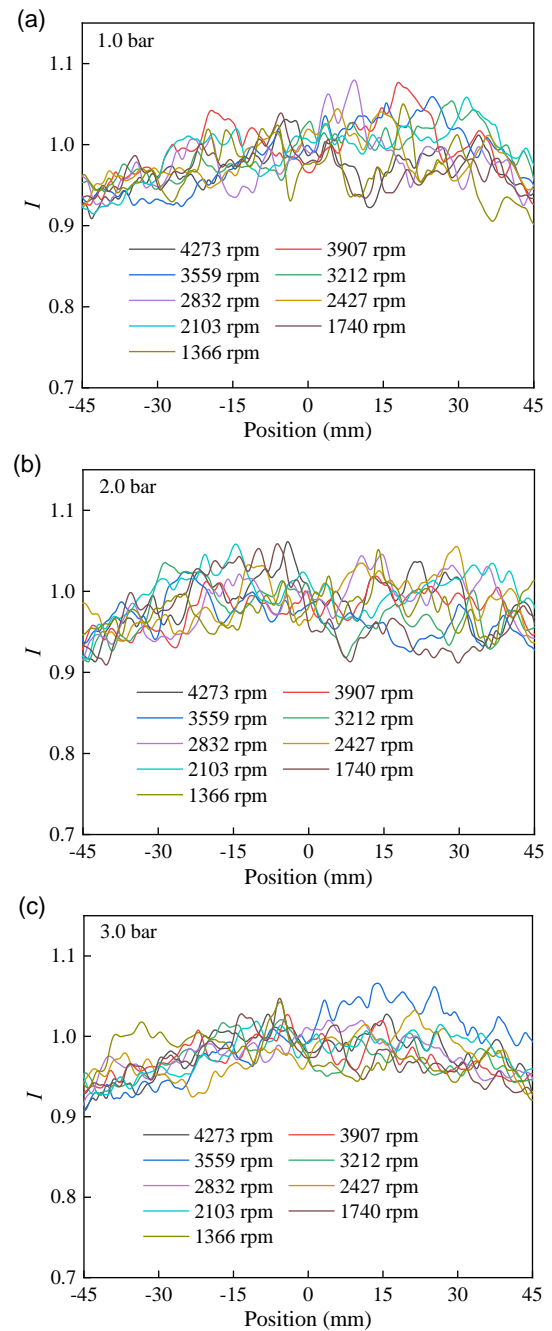


**Figure 6.** Isotropic ratio in the whole field of view. a)  $P=1.0$  bar; b)  $P=2.0$  bar; and c)  $P=3.0$  bar.

### 3.2. Influence of Turbulence and Diffusional–Thermal Instability

The flame was fully developed and unaffected by the pressure in the confined space when the radius of the flame was 35 mm. Therefore, the data at the flame radius of 35 mm were selected for further analysis. **Figure 7** depicts the variation in flame propagation speed of hydrogen-rich syngas at a flame radius of 35 mm under various pressures, equivalence ratios, hydrogen fractions, and turbulence intensities. The value of  $S_{T,35\text{ mm}}$

- $X_{H_2} = 55\%$   $\phi = 0.6$     ●  $X_{H_2} = 65\%$   $\phi = 0.6$     ▲  $X_{H_2} = 75\%$   $\phi = 0.6$
- $X_{H_2} = 55\%$   $\phi = 0.8$     ○  $X_{H_2} = 65\%$   $\phi = 0.8$     △  $X_{H_2} = 75\%$   $\phi = 0.8$
- ▣  $X_{H_2} = 55\%$   $\phi = 1.0$     ◊  $X_{H_2} = 65\%$   $\phi = 1.0$     ▽  $X_{H_2} = 75\%$   $\phi = 1.0$
- ▼  $X_{H_2} = 85\%$   $\phi = 0.6$     ◆  $X_{H_2} = 95\%$   $\phi = 0.6$
- ▽  $X_{H_2} = 85\%$   $\phi = 0.8$     ◇  $X_{H_2} = 95\%$   $\phi = 0.8$
- ▽  $X_{H_2} = 85\%$   $\phi = 1.0$     ◇  $X_{H_2} = 95\%$   $\phi = 1.0$

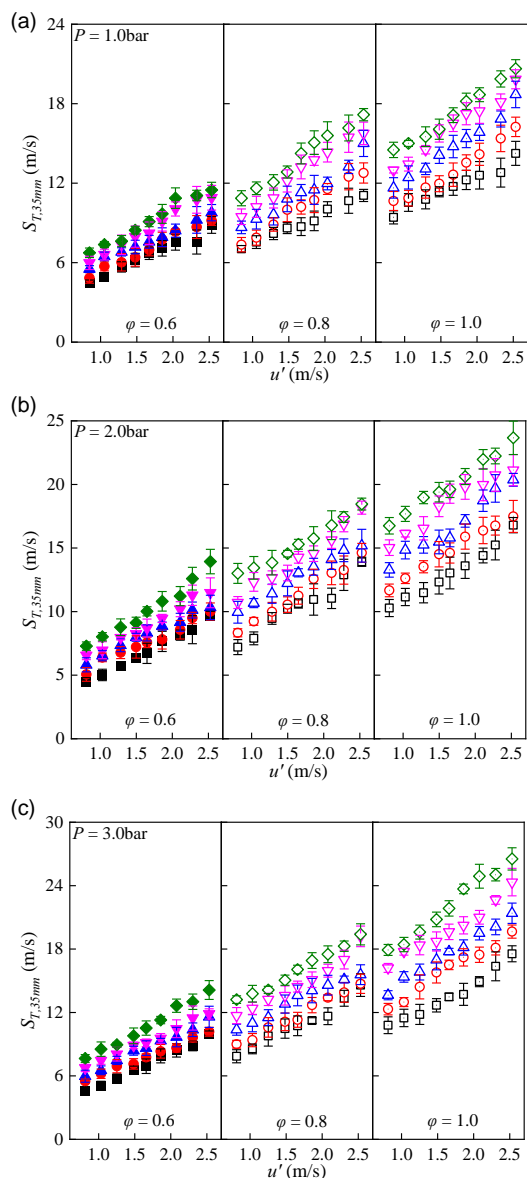


**Figure 7.**  $S_{T,35\text{ mm}}$  of hydrogen-rich syngas turbulent premixed flame. a)  $P = 1.0$  bar; b)  $P = 2.0$  bar; c)  $P = 3.0$  bar.

gradually increased as the turbulence intensity increased. With increased  $\phi$ , the value of  $S_{T,35\text{ mm}}$  also increased gradually. Comparing the effect of  $X_{H_2}$  on the propagation speed of the flame under the same conditions, it is found that the value of  $S_{T,35\text{ mm}}$  will also increase with the increase of  $X_{H_2}$ . By comparing the data of different pressures, it is found that the value of  $S_{T,35\text{ mm}}$  increased with the increase of pressure. This means that the increases in turbulence intensity, equivalence ratio, hydrogen

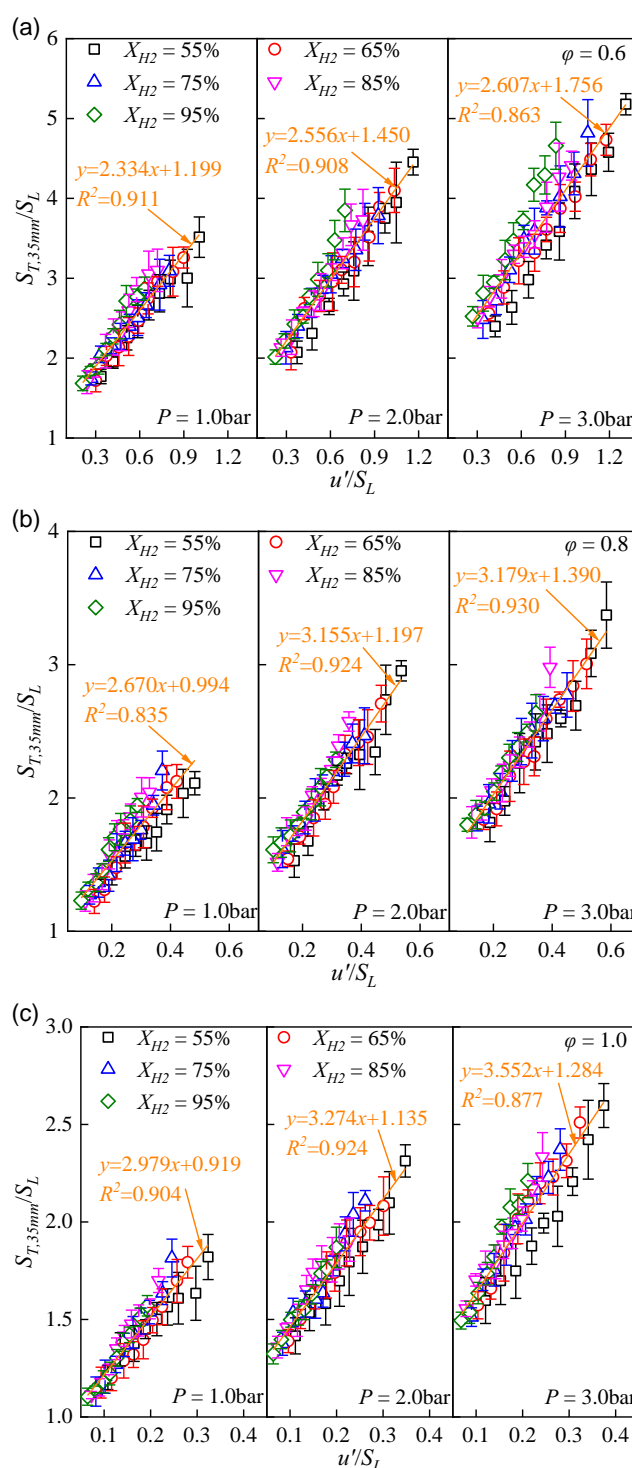


**Figure 8.** Effect of  $u'/S_L$  on  $S_{T,35\text{ mm}}/S_L$  under different equivalence ratios. a)  $\phi = 0.6$ ; b)  $\phi = 0.8$ ; and c)  $\phi = 1.0$ .

fraction, and pressure have a positive effect on the flame propagation speed.

**Figure 8** depicts the relationship between  $u'/S_L$  and  $S_{T,35\text{ mm}}/S_L$  under different equivalence ratios. It can be observed that the value of  $S_{T,35\text{ mm}}/S_L$  increased with the increase of  $u'/S_L$ ,



and showed a good linear association. With the increase of pressure, the value of  $S_{T,35\text{ mm}}/S_L$  increased gradually. With increased  $\phi$ , the values of  $S_{T,35\text{ mm}}/S_L$  and  $u'/S_L$  decreased. For the same equivalence ratio, the slope and intercept of the linear association between  $S_{T,35\text{ mm}}/S_L$  and  $u'/S_L$  increased with the increase of pressure. For the same pressure, with the increase of  $\phi$ , the slope of the linear association between  $S_{T,35\text{ mm}}/S_L$  and  $u'/S_L$  increased, while the intercept decreased.

Hydrogen-rich syngas contains two combustible gases of hydrogen and carbon monoxide. Therefore, the effective Lewis number ( $Le_{\text{eff}}$ ) proposed by Kwon et al.<sup>[52]</sup> is used to characterize the DT instability of hydrogen-rich syngas, as given by Equation (16).

$$Le_{\text{eff}} = 1 + \frac{q_{\text{H}_2}(Le_{\text{H}_2} - 1) + q_{\text{CO}}(Le_{\text{CO}} - 1)}{q} \quad (16)$$

where  $q_i$  and  $Le_i$  represent the heat release and Lewis number of  $\text{H}_2/\text{air}$  mixture and  $\text{CO}/\text{air}$  mixture, respectively, and  $q$  represents the total heat release of the mixture.

**Figure 9** shows the relationship between  $Le_{\text{eff}}$  and  $S_{T,35\text{ mm}}/S_L$  of hydrogen-rich syngas turbulent premixed flame under different turbulence intensities. With increased  $X_{\text{H}_2}$ , the value of  $Le_{\text{eff}}$  decreased gradually. As  $\phi$  increased, the value of  $Le_{\text{eff}}$  increased, while that of  $S_{T,35\text{ mm}}/S_L$  decreased gradually. With the increase of  $u'$ , the value of  $S_{T,35\text{ mm}}/S_L$  increased gradually. The results

also showed that the slope of  $S_{T,35\text{ mm}}/S_L$  with  $Le_{\text{eff}}$  increased with the increase of  $X_{\text{H}_2}$ .

**Figure 10** shows the relationship between  $Ka \cdot Le_{\text{eff}}$  and  $S_{T,35\text{ mm}}/S_L$  of hydrogen-rich syngas at different hydrogen fractions. The variation in  $Ka \cdot Le_{\text{eff}}$  and  $S_{T,35\text{ mm}}/S_L$  showed a power-function relationship between them. With the increase of  $Ka \cdot Le_{\text{eff}}$ , the value of  $S_{T,35\text{ mm}}/S_L$  increased gradually. With the decrease of  $\phi$ , the variation range of  $S_{T,35\text{ mm}}/S_L$  with  $Ka \cdot Le_{\text{eff}}$  increased gradually. With the increase of  $u'$ , the variation range of  $S_{T,35\text{ mm}}/S_L$  with  $Ka \cdot Le_{\text{eff}}$  increased gradually. As  $X_{\text{H}_2}$  increased, the value of  $Ka \cdot Le_{\text{eff}}$  decreased gradually, while the power-function coefficient between  $Ka \cdot Le_{\text{eff}}$  and  $S_{T,35\text{ mm}}/S_L$  increased gradually.

According to Equation (17), the Zel'dovich number is the dimensionless representation of the activation energy ( $E_a$ ) of a chemical reaction.

$$Ze = \frac{E_a(T_b - T_u)}{R(T_b)^2} \quad (17)$$

where  $R$  is the gas constant,  $T_b$  is the temperature of burnt gas, and  $T_u$  is the temperature of unburnt gas.

**Figure 11** demonstrates the relationship between  $Ze$  and  $u_{t,35\text{ mm}}/u_l$  of hydrogen-rich syngas at different pressures. The results showed that, under the same  $\phi$ , the value of  $Ze$  increased gradually with the decrease of hydrogen fraction, whereas  $u_{t,35\text{ mm}}/u_l$  exhibited an increasing trend. For the same hydrogen

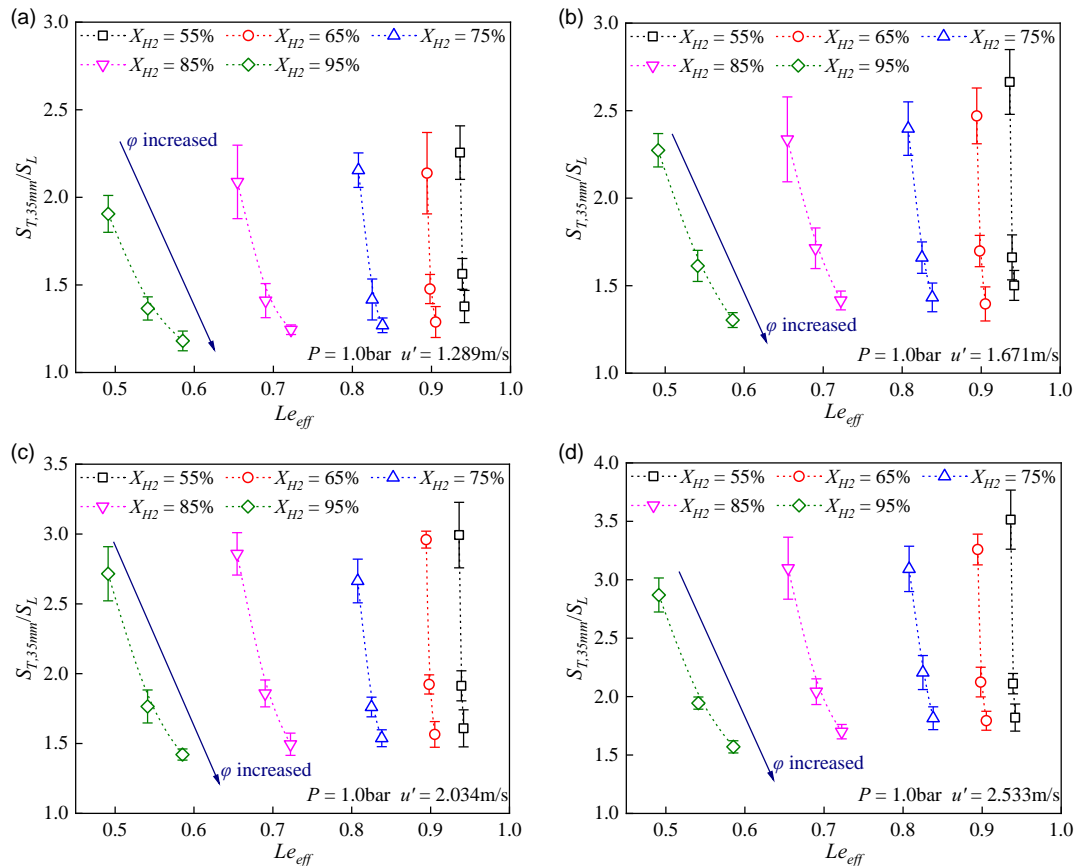


**Figure 9.** Effect of  $Le_{\text{eff}}$  on  $S_{T,35\text{ mm}}/S_L$  under different turbulence intensities. a)  $1.289\text{ m s}^{-1}$ ; b)  $1.671\text{ m s}^{-1}$ ; c)  $2.034\text{ m s}^{-1}$ ; and d)  $2.533\text{ m s}^{-1}$ .

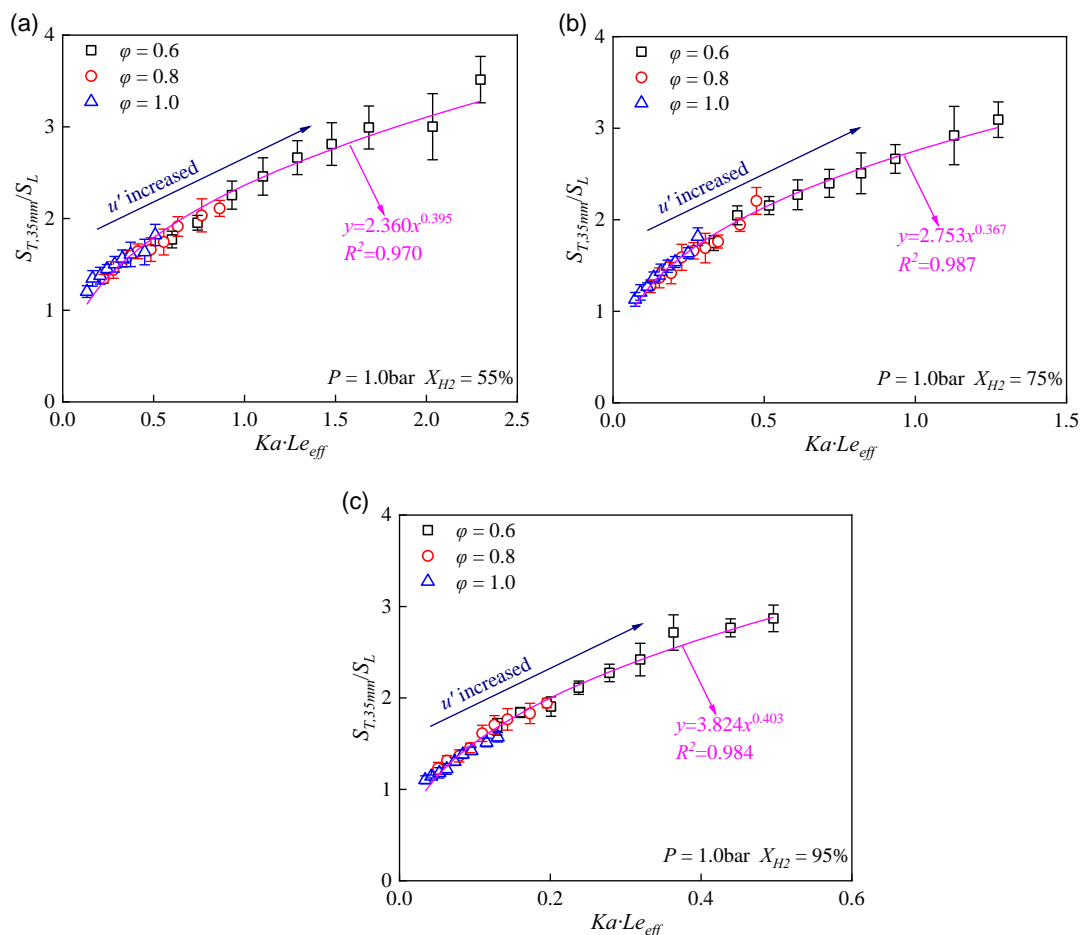


**Figure 10.** Effect of  $Ka \cdot Le_{eff}$  on  $S_{T,35mm}/S_L$  under different hydrogen fractions. a)  $X_{H_2} = 55\%$ ; b)  $X_{H_2} = 75\%$ ; and c)  $X_{H_2} = 95\%$ .

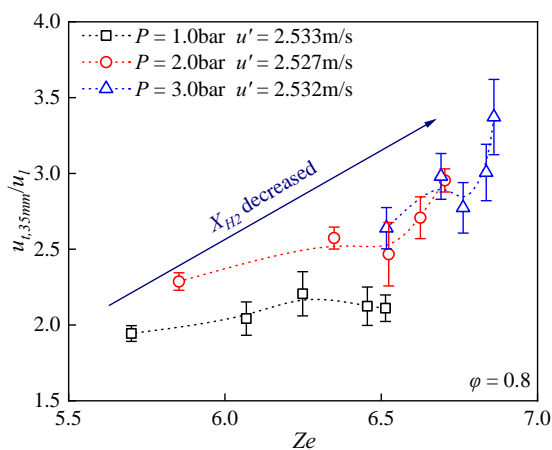


**Figure 11.** Effect of  $Ze$  on  $u_{t,35mm}/u_1$  under different pressures.

fraction, both  $Ze$  and  $u_{t,35mm}/u_1$  increased with the increase of pressure.

Figure 12 shows the association between  $Ka$  and  $u_{t,35mm}/u'$  under different hydrogen fractions. The results showed that the value of  $u_{t,35mm}/u'$  decreased gradually with the increase of  $Ka$ , and there was a power-function relationship between

$u_{t,35mm}/u'$  and  $Ka$ . As  $u'$  increased, the value of  $Ka$  increased gradually, while that of  $u_{t,35mm}/u'$  decreased. As  $\varphi$  increased, the value of  $Ka$  gradually decreased, while that of  $u_{t,35mm}/u'$  increased. With the increase of  $X_{H_2}$ , the value of  $Ka$  gradually decreased, while that of  $u_{t,35mm}/u'$  increased. Meanwhile, the power-function coefficient between  $u_{t,35mm}/u'$  and  $Ka$  gradually increased, whereas the power gradually decreased.

Figure 13 shows the association between  $(Da/Le_{eff})^{0.5}$  and  $S_{T,35mm}/u'$  under different equivalence ratios. The value of  $S_{T,35mm}/u'$  increased with the increase of  $(Da/Le_{eff})^{0.5}$ , and showed a power-function relationship. With increased pressure, the values of  $(Da/Le_{eff})^{0.5}$  and  $S_{T,35mm}/u'$  increased gradually. With the increase of  $X_{H_2}$ , the value of  $(Da/Le_{eff})^{0.5}$  increased, while that of  $S_{T,35mm}/u'$  increased gradually. Meanwhile, the increasing range of  $S_{T,35mm}/u'$  increased gradually. As  $\varphi$  increased, the values of  $(Da/Le_{eff})^{0.5}$  and  $S_{T,35mm}/u'$  increased gradually, whereas the power and power-function coefficient between  $S_{T,35mm}/u'$  and  $(Da/Le_{eff})^{0.5}$  increased as well.

## 4. Conclusions

A constant volume bomb which can create homogeneity and isotropy turbulent flow field was built. The effects of turbulence

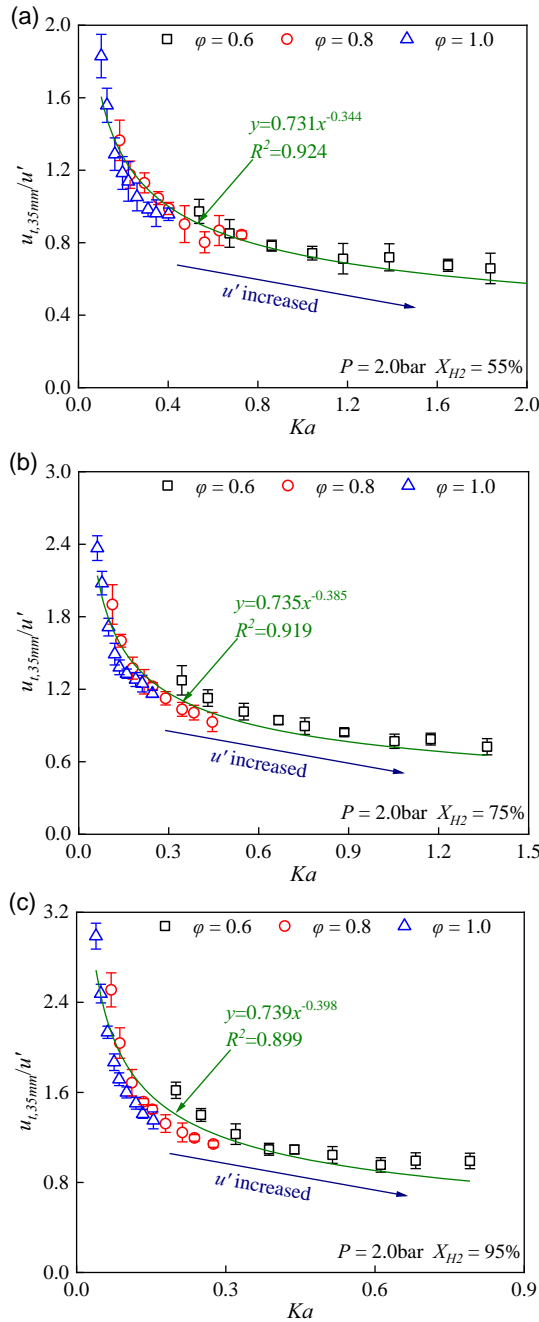


**Figure 12.** Effect of  $Ka$  on  $u_{t,35\text{ mm}}/u'$  under different hydrogen fractions. a)  $X_{H_2} = 55\%$ ; b)  $X_{H_2} = 75\%$ ; and c)  $X_{H_2} = 95\%$ .

and DT instability of a hydrogen-rich syngas turbulent premixed flame were investigated in this study at various hydrogen fractions, turbulence intensities, pressures, and equivalence ratios. The findings of the study lead to the following conclusions: 1) Through the calibration of turbulent flow field, it was found that  $u'$  increased with the increase of fan speed. In addition, the change of pressure had no obvious effect on  $u'$  and  $L_T$ . The quantitative analysis of homogeneity and isotropy of the turbulent flow field showed that the turbulence field in the

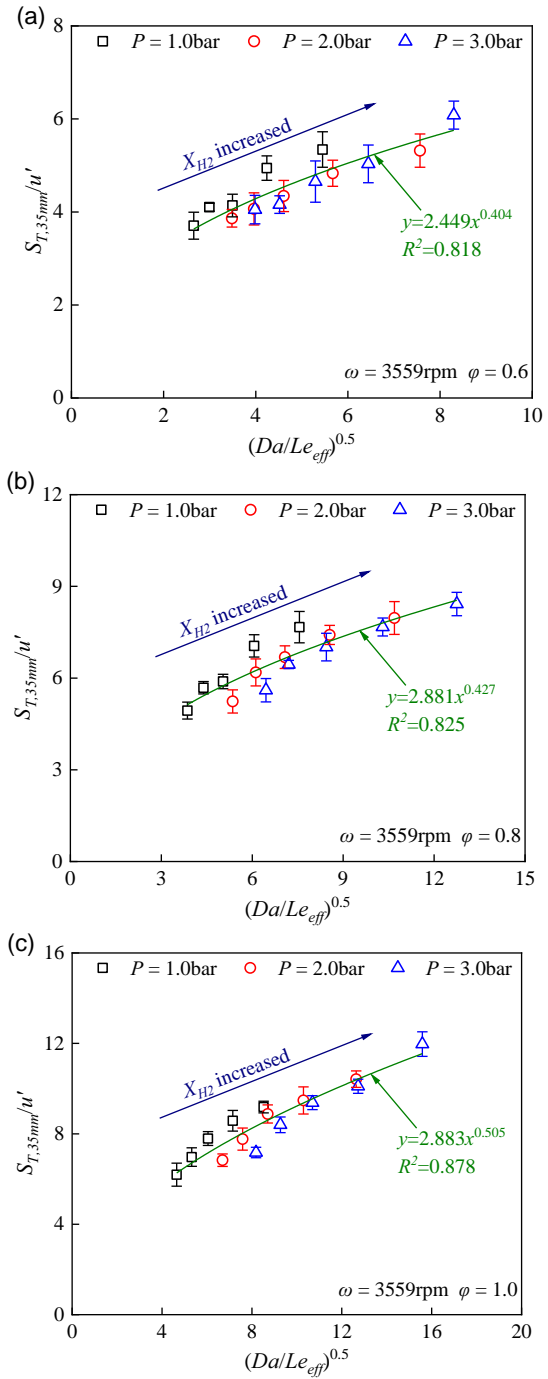


**Figure 13.** Effect of  $(Da/Le_{eff})^{0.5}$  on  $S_{T,35\text{ mm}}/u'$  under different equivalence ratios. a)  $\phi = 0.6$ ; b)  $\phi = 0.8$ ; and c)  $\phi = 1.0$ .

constant volume bomb was homogeneous and isotropic in the studied experimental setup. This provides an important guarantee for further turbulent premixed combustion experiments. 2) The value of  $S_{T,35\text{ mm}}$  increased gradually while turbulence intensity, equivalence ratio, hydrogen fraction, or pressure increased. Moreover, the value of  $S_{T,35\text{ mm}}/S_L$  increased with the increase of  $u'/S_L$ , and showed a good linear association.

With the increase of  $X_{H_2}$ , the values of  $Le_{eff}$  and  $Ka \cdot Le_{eff}$  decreased gradually. When  $\varphi$  increased, the value of  $Le_{eff}$  increased, while that of  $S_{T,35\text{ mm}}/S_L$  decreased. Moreover, the value of  $S_{T,35\text{ mm}}/S_L$  will increase with the increase in pressure. 3) As  $u'$  increased, the value of  $Ka$  increased, while that of  $u_{t,35\text{ mm}}/u'$  decreased. While  $X_{H_2}$  increased, the power–function coefficient between  $u_{t,35\text{ mm}}/u'$  and  $Ka$  increased and the power decreased. As equivalence ratio or pressure increased, the values of  $(Da/Le_{eff})^{0.5}$  and  $S_{T,35\text{ mm}}/u'$  increased gradually. With the increase of  $u'$ , the values of  $(Da/Le_{eff})^{0.5}$  and  $S_{T,35\text{ mm}}/u'$  decreased gradually. When  $\varphi$  decreased, the power and the power–function coefficient between  $S_{T,35\text{ mm}}/u'$  and  $(Da/Le_{eff})^{0.5}$  increased. 4) By conducting research on turbulent premixed flames of hydrogen-rich syngas in a constant volume bomb, its propagation process can be clarified. The coupling effect of turbulence and flame inherent instabilities on the hydrogen-rich syngas turbulent premixed flames has been deeply analyzed, which also provides a basis for analyzing other fuels. In addition, the study of this paper can not only provide important data support for the clean and efficient utilization of hydrogen-rich syngas, but also provide reference for the design and development of related burners.

## Acknowledgements

This work is supported by the Fundamental Research Funds for the Central Universities (Grant No.2022YJ084) and the National Natural Science Foundation of China (Grant No. 51706014).

## Conflict of Interest

The authors declare no conflict of interest.

## Data Availability Statement

Research data are not shared.

## Keywords

diffusional-thermal instability, flame propagation speed, hydrogen-rich syngas, turbulent premixed flame

Received: July 31, 2023

Revised: September 7, 2023

Published online: October 25, 2023

- [1] P. Zhao, L. Zeng, P. Li, H. Lu, H. Hu, C. Li, M. Zheng, H. Li, Z. Yu, D. Yuan, J. Xie, Q. Huang, Y. Qi, *Energy* **2022**, 238, 121934.
- [2] C. Movileanu, M. Mitu, V. Giurcan, D. Razus, D. Oancea, *Fuel* **2020**, 274, 117836.
- [3] D. M. Al-Mohannadi, P. Linke, *Energy Technol.* **2020**, 8, 1901381.
- [4] J. Fang, C. Xiong, M. Feng, Y. Wu, D. Liu, *Appl. Energy* **2022**, 312, 118809.
- [5] D. Pashchenko, *Renewable Sustainable Energy Rev.* **2023**, 173, 113117.
- [6] D. Pashchenko, *Int. J. Hydrogen Energy* **2020**, 45, 19996.
- [7] J. Yang, S. Dong, L. Xie, Q. Cen, D. Zheng, L. Ma, Q. Dai, *Energy* **2023**, 283, 128499.
- [8] Q. Wang, G. Wang, W. Li, B. Chen, *Energy Technol.* **2016**, 4, 751.
- [9] B. V. Ayodele, S. I. Mustapa, *Front Energy Res.* **2019**, 7, 118.
- [10] F. Zhang, T. Zirwes, H. Nawroth, P. Habisreuther, H. Bockhorn, C. O. Paschereit, *Energy Technol.* **2017**, 5, 1045.
- [11] H. Shehab, H. Watanabe, Y. Minamoto, R. Kurose, T. Kitagawa, *Combust. Flame* **2022**, 238, 111888.
- [12] Q. Fan, X. Liu, L. Xu, A. A. Subash, C. Brackmann, M. Alden, X. Bai, Z. Li, *Combust. Flame* **2022**, 238, 111943.
- [13] G. P. Zhang, G. X. Li, H. M. Li, J. C. Lv, *Energy* **2022**, 246, 123370.
- [14] A. Qamareen, S. S. Alam, M. A. Ansari, *Energy Technol.* **2021**, 9, 2100294.
- [15] S. S. Shy, C. C. Liu, J. Y. Lin, L. L. Chen, A. N. Lipatnikov, S. I. Yang, *Proc. Combust. Inst.* **2015**, 35, 1509.
- [16] X. Cai, J. Wang, Z. Bian, H. Zhao, H. Dai, Z. Huang, *Combust. Flame* **2020**, 215, 364.
- [17] Y. Nie, J. Wang, W. Zhang, M. Chang, M. Zhang, Z. Huang, *Fuel* **2019**, 242, 607.
- [18] H. C. Cutcher, R. S. Barlow, G. Magnotti, A. R. Masri, *Combust. Flame* **2018**, 194, 439.
- [19] A. R. W. Macfarlane, M. J. Dunn, M. Juddoo, A. R. Masri, *Proc. Combust. Inst.* **2017**, 36, 1661.
- [20] M. T. Nguyen, S. S. Shy, Y. R. Chen, B. L. Lin, S. Y. Huang, C. C. Liu, *Proc. Combust. Inst.* **2021**, 38, 2801.
- [21] F. Zhang, T. Baust, T. Zirwes, J. Denev, P. Habisreuther, N. Zarzalis, H. Bockhorn, *Energy Technol.* **2017**, 5, 1055.
- [22] G. P. Zhang, G. X. Li, H. M. Li, J. C. Lv, *Int. J. Hydrogen Energy* **2022**, 47, 610.
- [23] J. Sidey, E. Mastorakos, *Proc. Combust. Inst.* **2017**, 36, 1721.
- [24] M. M. Kamal, B. Coriton, R. Zhou, J. H. Frank, S. Hochgreb, *Proc. Combust. Inst.* **2017**, 36, 1957.
- [25] K. H. H. Goh, P. Geipel, R. P. Lindstedt, *Combust. Flame* **2014**, 161, 2419.
- [26] G. Darrieus, *La Tech. Mod.* **1938**, 30, 18.
- [27] L. D. Landau, *Acta Physicochim.* **1944**, 19, 77.
- [28] G. H. Markstein, *J. Chem. Phys.* **1949**, 17, 428.
- [29] J. Manton, G. Von Elbe, B. Lewis, *J. Chem. Phys.* **1952**, 20, 153.
- [30] J. Wang, F. Matsuno, M. Okuyama, Y. Ogami, H. Kobayashi, Z. Huang, *Proc. Combust. Inst.* **2013**, 34, 1429.
- [31] M. Zhang, J. Wang, W. Jin, Z. Huang, H. Kobayashi, L. Ma, *Combust. Flame* **2015**, 162, 2087.
- [32] P. Venkateswaran, A. Marshall, J. Seitzman, T. Lieuwen, *Proc. Combust. Inst.* **2013**, 34, 1527.
- [33] J. Goulier, A. Comandini, F. Halter, N. Chaumeix, *Proc. Combust. Inst.* **2016**, 36, 2823.
- [34] W. Jin, C. Ren, J. Li, J. Wang, Y. Yan, *Fuel* **2022**, 310, 122292.
- [35] F. Creta, P. E. Lapenna, R. Lamioni, N. Fogla, M. Matalon, *Combust. Flame* **2020**, 216, 256.
- [36] Y. Li, M. Bi, W. Gao, Y. Zhou, L. Huang, *J. Loss Prevent. Process. Ind.* **2020**, 64, 104078.
- [37] K. K. J. R. Dinesh, H. Shalaby, K. H. Luo, J. A. V. Oijen, D. Thevenin, *Int. J. Hydrogen Energy* **2016**, 41, 18231.
- [38] K. K. J. R. Dinesh, H. Shalaby, K. H. Luo, J. A. V. Oijen, D. Thevenin, *Int. J. Hydrogen Energy* **2016**, 41, 21516.
- [39] T. M. Vu, W. S. Song, J. Park, D. S. Bae, H. S. You, *Int. J. Hydrogen Energy* **2011**, 36, 12058.
- [40] L. Berger, A. Attili, H. Pitsch, *Combust. Flame* **2022**, 240, 111935.
- [41] L. Berger, A. Attili, H. Pitsch, *Combust. Flame* **2022**, 240, 111936.
- [42] S. Kadowaki, H. Suzuki, H. Kobayashi, *Proc. Combust. Inst.* **2005**, 30, 169.
- [43] Z. Liu, S. Yang, C. K. Law, A. Saha, *Proc. Combust. Inst.* **2019**, 37, 2611.
- [44] D. Pashchenko, *Int. J. Hydrogen Energy* **2017**, 42, 29545.
- [45] M. Weiß, N. Zarzalis, R. Suntz, *Combust. Flame* **2008**, 154, 671.
- [46] S. Ravi, S. J. Peltier, E. L. Petersen, *Exp. Fluids* **2013**, 54, 1424.

- [47] H. Zhao, J. Wang, X. Cai, Z. Bian, H. Dai, Z. Huang, *Front. Energy* **2022**, 16, 973.
- [48] T. Kitagawa, T. Nakahara, K. Maruyama, K. Kado, A. Hayakawa, S. Kobayashi, *Int. J. Hydrogen Energy* **2008**, 33, 5842.
- [49] B. Galmiche, N. Mazellier, F. Halter, F. Foucher, *Exp. Fluids* **2014**, 55, 1636.
- [50] S. Xu, S. Huang, R. Huang, W. Wei, X. Cheng, Y. Ma, Y. Zhang, *Appl. Therm. Eng.* **2017**, 110, 346.
- [51] S. Chaudhuri, A. Saha, C. K. Law, *Proc. Combust. Inst.* **2015**, 35, 1331.
- [52] O. C. Kwon, G. Rozenchan, C. K. Law, *Proc. Combust. Inst.* **2002**, 29, 1775.
- [53] E. S. Semenov, *Combust. Explos. Shock Waves* **1965**, 1, 57.
- [54] T. D. Fansler, E. G. Groff, *Combust. Flame* **1990**, 80, 350.
- [55] V. Sick, M. R. Hartman, V. S. Arpaci, R. W. Anderson, *Combust. Flame* **2001**, 127, 2119.
- [56] A. Smallbone, K. Tsuneyoshi, T. Kitagawa, *J. Therm. Sci. Technol.* **2006**, 1, 31.
- [57] C. C. Liu, S. S. Shy, H. C. Chen, M. W. Peng, *Proc. Combust. Inst.* **2011**, 33, 1293.
- [58] J. Goulier, N. Chaumeix, F. Halter, N. Meynet, A. Bentaib, *Nucl. Eng. Des.* **2017**, 312, 214.
- [59] D. Bradley, M. Lawes, M. E. Morsy, *Fuel* **2019**, 243, 423.
- [60] Y. Jiang, G. Li, H. Li, G. Zhang, J. Lv, *Energy Fuel* **2019**, 33, 12736.
- [61] O. A. Mannaa, M. S. Mansour, S. H. Chung, W. L. Roberts, *Combust. Sci. Technol.* **2021**, 193, 1231.